



Chromium-modified $\text{Bi}_4\text{Ti}_3\text{O}_{12}$ photocatalyst: Application for hydrogen evolution and pollutant degradation

Zhiwu Chen^{a,*}, Xunyang Jiang^a, Chengbin Zhu^a, Chunkai Shi^{b,*}

^a College of Materials Science and Engineering, South China University of Technology, Guangzhou 510640, China

^b Department of Chemistry, New Mexico Tech., Socorro, NM, 87801, USA

ARTICLE INFO

Article history:

Received 5 February 2016

Received in revised form 8 June 2016

Accepted 10 June 2016

Available online 14 June 2016

Keywords:

Chromium-modified $\text{Bi}_4\text{Ti}_3\text{O}_{12}$

Hydrogen production from alcohol–water mixture

MO degradation

Nanosheets

Photocatalysis

ABSTRACT

Novel chromium-modified $\text{Bi}_4\text{Ti}_3\text{O}_{12}$ photocatalyst ($\text{Bi}_4\text{Ti}_{3-x}\text{Cr}_x\text{O}_{12}$, $x = 0-0.5$) was developed by a facile sol-gel hydrothermal process with low reaction temperature. The XRD, SEM, TEM, and XPS analyses indicated the formation of the single-crystalline, rectangular, and {001} facet-exposed $\text{Bi}_4\text{Ti}_{3-x}\text{Cr}_x\text{O}_{12}$ nanosheets. Their average side lengths and thickness progressively decreased with increase in the Cr content, and the minimal side length and thickness for $\text{Bi}_4\text{Ti}_{2.6}\text{Cr}_{0.4}\text{O}_{12}$ are 95 and 15 nm, respectively. With more addition of Cr content, sample showed significant particle agglomeration even though some of small nanosheets were observed. The UV–vis study revealed a reduction in the band gap of $\text{Bi}_4\text{Ti}_{3-x}\text{Cr}_x\text{O}_{12}$ and enhanced photoabsorption in the visible light region, compared to the calcined $\text{Bi}_4\text{Ti}_3\text{O}_{12}$. The photoluminescence and electrochemical impedance spectroscopy results displayed a decreased recombination of photogenerated charges in the Cr-modified $\text{Bi}_4\text{Ti}_3\text{O}_{12}$ compared to Cr-free one. The photocatalysts were optimized for both maximum hydrogen generation from alcohol–water mixture and methyl orange (MO) degradation in an aqueous solution under visible light irradiation. As a result, addition of Cr effectively improves photocatalytic performance of $\text{Bi}_4\text{Ti}_3\text{O}_{12}$. $\text{Bi}_4\text{Ti}_{2.6}\text{Cr}_{0.4}\text{O}_{12}$, the optimal photocatalyst, showed highly stable reusability as a hydrogen generator. The photocatalyst reached as much as $117 \mu\text{mol g}^{-1} \text{h}^{-1}$ hydrogen evolution rate under 240 min of irradiation, which was ~ 2.85 times that of the $\text{Bi}_4\text{Ti}_3\text{O}_{12}$ nanosheet. The hydrogen yields of the $\text{Bi}_4\text{Ti}_{2.6}\text{Cr}_{0.4}\text{O}_{12}$ using various alcohol–water mixtures decreased in the order: isopropanol > ethanol > methanol. The optimal photocatalyst also showed up to 0.01003 min^{-1} of average apparent rate constant in the MO degradation, about 3 times that of the Cr-free nanosheet. The improved photocatalytic performance of the Cr-modified $\text{Bi}_4\text{Ti}_3\text{O}_{12}$ is attributed to its strong absorption in visible light region, small nanosheet size, exposed {001} facets as well as the low recombination rate or the high separation efficiency for photogenerated electron–hole pairs.

© 2016 Elsevier B.V. All rights reserved.

1. Introduction

Visible-light-driven photocatalysis has received worldwide attention in that it shows great potential in applying sun light to eliminate environmental pollutants and to produce energy and value-added chemicals [1–3]. Oxides are desirable catalysts to facilitate these photocatalytic processes since they are stable under usual operating conditions [4]. To date, a large number of metal oxides have been explored for the photocatalytic processes, specifically photocatalytic hydrogen production through splitting water [5–8]. Among all metal oxides, TiO_2 , a typical n-type semiconductor, has been widely used as a photocatalyst for energy conversion

and dye pollutant elimination thanks to its high activity and stability, low cost, availability and nontoxicity [9–11]. However, TiO_2 as a photocatalyst can only be activated under UV light irradiation ($\lambda < 388 \text{ nm}$) due to its large band gap (about 3.2 eV), which accounts for less than 5% of solar energy [12]. Hence, many efforts have been made to extend the photoresponse of TiO_2 to the visible-light region and to boost the separation of photoexcited charge carriers, including doping extraneous elements, such as N and B, into the lattices of TiO_2 [13,14], coupling with visible light absorbers [15,16], semiconductor (CdS) [17], and surface sensitizer (zinc phthalocyanine) [18]. However, a discrete doping level only absorbs the small amount of visible light [19], and some of dopants act as the trapping center for photogenerated charge carriers [20]. In addition, the formation of composites generally requires complex synthesis routes, increases the potential instability of catalyst due to introduced layer, and creates the possibility of inefficient charge

* Corresponding authors.

E-mail addresses: chenzw@scut.edu.cn (Z. Chen), chunkaishi@yahoo.com, chunkaishi@gmail.com (C. Shi).

separation owing to multistep electron transport process. Such a doped catalyst shows a limited enhanced photocatalytic activity. Thus, from a viewpoint of both the catalyst's stability and efficient electron/hole separation, the most reliable candidates for visible-light-driven photocatalysts would be single-phase metal oxides [21–23].

Bismuth titanate ($\text{Bi}_4\text{Ti}_3\text{O}_{12}$), well known as good optical, ferroelectric, and optoelectronic materials [24–26], has also been explored as a visible-light-driven photocatalyst due to its unique physicochemical properties and photocatalytic activity in the degradation for organic pollutants and hydrogen generation from water splitting. For example, $\text{Bi}_4\text{Ti}_3\text{O}_{12}$ nanofibers [27], particulates [28–30], platelets [31], and films [32] have been reported as active and visible-light-driven photocatalysts for either energy development or degradation of organic pollutants. The structure of $\text{Bi}_4\text{Ti}_3\text{O}_{12}$ shows high stability under these harsh photocatalytic reaction conditions. Unfortunately, the overall photocatalytic efficiency of these $\text{Bi}_4\text{Ti}_3\text{O}_{12}$ nanomaterials still needs to be improved because of the rapid recombination of electron–hole pairs after visible-light excitation. Obviously, one of the potential goals is to develop highly active $\text{Bi}_4\text{Ti}_3\text{O}_{12}$ -based single-phase photocatalysts with significantly improved visible-light absorbance and low recombination rate of photogenerated charge carriers.

Achieving good crystallinity with the addition of external elements in a metal oxide is a huge challenge. As a member of the Aurivillius family compounds, $\text{Bi}_4\text{Ti}_3\text{O}_{12}$ is well known to have a layered perovskite structure with thermodynamical stability. Its two cationic sites can be partly substituted by external elements, and its basic perovskite structure also remains unchanged. This allows for its optical absorbance and photocatalytic properties within the host perovskite structure can be tuned much effectively. For example, $\text{Bi}_{3.25}\text{La}_{0.75}\text{Ti}_3\text{O}_{12}$ nanowires and $\text{Bi}_{3.25}\text{Sm}_{0.75}\text{Ti}_3\text{O}_{12}$ nanostructures are developed, and exhibit visible-light activity towards degradation of organic pollutants [33,34]. Recently, chromium-doped $\text{Bi}_4\text{Ti}_3\text{O}_{12}$ catalyst, synthesized by first sol-gel process and subsequent calcination treatment of 750°C , demonstrates photocatalytic production of H_2 under visible-light irradiation [35]. Although the partial replacement of the Bi and Ti in $\text{Bi}_4\text{Ti}_3\text{O}_{12}$ by external metal elements can be easily performed using conventional solid ion reaction method, as-prepared products show compositional inhomogeneity and large particle size due to high calcination temperature (usually $\geq 800^\circ\text{C}$), insufficient absorbance in the visible light region, and thus, low photocatalytic performance.

Recently, our team applies a novel synthesis method, sol-gel hydrothermal technique with the reaction temperature as low as 160°C , to prepare highly crystalline and size-controlled $\text{Bi}_4\text{Ti}_3\text{O}_{12}$ nanosheets, which exhibit enhanced photocatalytic activity in the visible-light-driven Rhodamine B degradation than sample conventionally calcined at 800°C [36]. Inspired by the novel synthesis technique, incorporating an additional element into the $\text{Bi}_4\text{Ti}_3\text{O}_{12}$ nanosheet is designed to further improve its absorbance in visible-light region and also remain its crystalline perfection. Specifically, a modification of $\text{Bi}_4\text{Ti}_3\text{O}_{12}$ nanosheets using chromium is investigated. The optical, surface, structural, morphology and photocatalytic properties of the Cr-modified $\text{Bi}_4\text{Ti}_3\text{O}_{12}$ nanosheets have been systematically examined. The catalysts, depending on added different chromium content, show an improvement in the visible light absorption compared to Cr-free sample. The photocatalytic hydrogen generation and methyl orange degradation studied using the synthesized catalysts demonstrates an enhancement in the catalytic performance until an optimum concentration of chromium was reached.

2. Experimental procedure

2.1. Catalyst preparation

$\text{Bi}_4\text{Ti}_{3-x}\text{Cr}_x\text{O}_{12}$ nanosheets were prepared via sol-gel synthesis and subsequent hydrothermal processing. First, according to the composition of $\text{Bi}_4\text{Ti}_{3-x}\text{Cr}_x\text{O}_{12}$ ($x=0-0.5$), solution A was obtained by dissolving the corresponding ration of $\text{Bi}(\text{NO}_3)_3 \cdot 5\text{H}_2\text{O}$ (0.02 mol) and $\text{Cr}(\text{NO}_3)_3 \cdot 9\text{H}_2\text{O}$ in 15 ml acetic acid simultaneously, and solution B was obtained by dissolving stoichiometric amount of $\text{Ti}(\text{C}_4\text{H}_9\text{O})_4$ in 15 ml ethylene glycol monomethylether under stirring at room temperature. All reagents were of analytical grade. Solution B was slowly added into solution A dropwise, and the mixture was vigorously stirred for 2 h, resulting in a homogeneous sol. The sol was stabilized when its concentration was adjusted to 0.1 M by adding 10 ml acetic acid and 10 ml ethylene glycol monomethylether, before being heated to 80°C for 24 h to produce dry gel. The gel was added to 75 ml of a 3 M NaOH solution to form a suspension, followed by pouring into a Teflon-lined stainless steel autoclave (volume of 100 ml) filled to 80% of capacity and subjected to hydrothermal treatment at 200°C for 16 h unless otherwise stated. Finally, the synthesized product was cooled down, filtered, washed with distilled water, and dried at room temperature. For comparison, $\text{Bi}_4\text{Ti}_3\text{O}_{12}$ powders were also prepared via conventional solid-state reaction among Bi_2O_3 and TiO_2 at 850°C for 2 h, as reported elsewhere [37].

2.2. Characterization

Crystalline structures of samples were examined using an X-ray diffractometer (XRD, D/Max-3C, Rigaku Co.) with Ni-filtered Cu K α radiation ($\lambda = 1.5418 \text{ \AA}$) in θ - 2θ scan mode, run at 40 kV and 30 mA. The 2θ range and step scan rate were $13-60^\circ$ and $0.01^\circ/\text{s}$, respectively.

Morphology of sample was observed using a scanning electron microscopy (SEM, LEO 1530 VP, Leo Ltd.) with accelerating voltage of 20 kV, and its composition was examined using energy dispersive spectroscopy (EDS) attached to the SEM. High resolution transmission electron microscopy (HRTEM) of the synthesized products was carried out on a JEOL-2011 instrument with accelerating voltage of 200 kV. The samples were prepared by dispersing $\text{Bi}_4\text{Ti}_{3-x}\text{Cr}_x\text{O}_{12}$ powders in anhydrous ethanol with sonication, and dripping on carbon-coated Cu grids.

The chemical states of samples were determined using an X-ray photoelectron spectrometer (XPS Axis uhru DCD, UK) with a monochromatic Mg K α X-ray source. All binding energies were referenced to the C 1s peak at 284.8 eV of the adventitious surface carbon.

The diffuse reflection spectra of the $\text{Bi}_4\text{Ti}_{3-x}\text{Cr}_x\text{O}_{12}$ nanosheets was analyzed using a UV-vis spectrophotometer (Model lambda 35, PerkinElmer) with an integrating sphere in the range of 250–800 nm, and BaSO_4 was used as the reference.

Photoluminescence (PL) spectra of sample was recorded using a PerkinElmer LS55 fluorescence spectrometer with the excitation wavelength of 320 nm at room temperature. The sample was pressed into a thin disk and fixed on a quartz cell.

Electrochemical impedance spectroscopy (EIS) of sample was conducted using a CHI 660 electrochemical workstation (CH Instruments, Inc., Austin, USA) with frequencies between 1×10^{-5} and 100 kHz and a potential of 0.17 V at room temperature. All measurements were based on a three-electrode system with a $\text{Bi}_4\text{Ti}_{3-x}\text{Cr}_x\text{O}_{12}$ electrode (see below for preparation) as the working electrode, a Ag/AgCl (3 M KCl) electrode as the reference electrode and a platinum wire as the auxiliary electrode. 0.1 M KCl and 0.1 M $\text{K}_3[\text{Fe}(\text{CN})_6]/\text{K}_4[\text{Fe}(\text{CN})_6]$ in a 1:1 mixture were used as the detecting electrolyte. A 300 W Xe lamp held at 10 cm from the

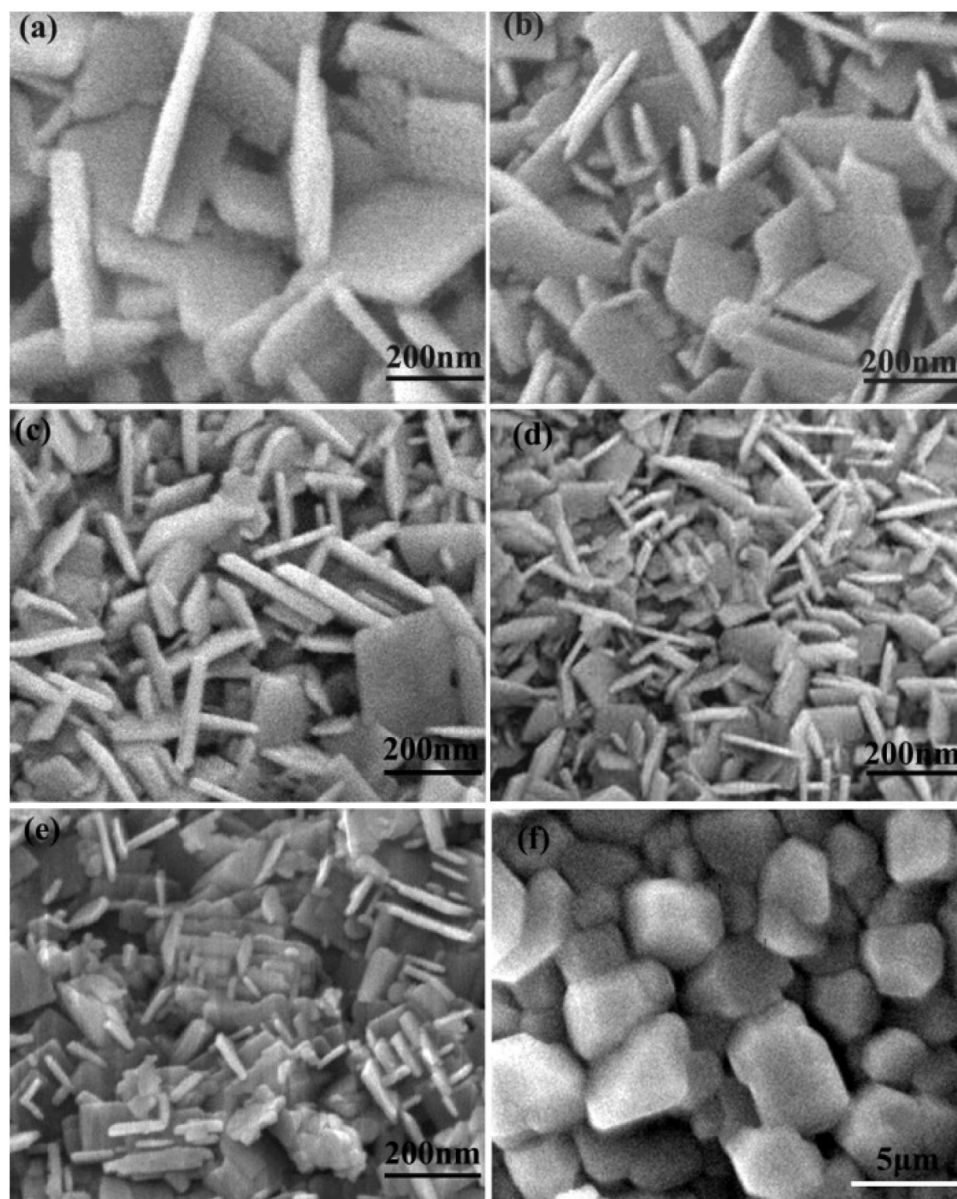


Fig. 1. SEM images of the $\text{Bi}_4\text{Ti}_{3-x}\text{Cr}_x\text{O}_{12}$ synthesized by sol-gel hydrothermal process at 200 °C: (a) $x = 0.0$, (b) $x = 0.15$, (c) $x = 0.30$, (d) $x = 0.40$, (e) $x = 0.50$, and (f) SEM image of $\text{Bi}_4\text{Ti}_3\text{O}_{12}$ synthesized by a conventional solid-state calcination at 850 °C.

quartz cell with a 420 nm UV filter was used as the visible-light source. The $\text{Bi}_4\text{Ti}_{3-x}\text{Cr}_x\text{O}_{12}$ electrodes were prepared as follow: First, 5 mg of $\text{Bi}_4\text{Ti}_{3-x}\text{Cr}_x\text{O}_{12}$ nanosheets was added to 0.5 ml solution containing 0.15 ml of pure ethyl alcohol ($\text{CH}_3\text{CH}_2\text{OH}$) and 0.35 ml of 5% Nafion DE 520 solution (EW is 1000, DuPont). The mixture was ultrasonically dispersed for 20 min. Then, 0.1 ml of the well-dispersed $\text{Bi}_4\text{Ti}_{3-x}\text{Cr}_x\text{O}_{12}$ slurry was cast onto cleaned ITO glass substrates ($<7 \Omega^{-2}$) to form uniform film electrodes. The $\text{Bi}_4\text{Ti}_{3-x}\text{Cr}_x\text{O}_{12}$ electrodes were finally obtained after sintering at 100 °C for 2 h.

2.3. Photocatalytic activity

The photocatalytic H_2 evolution from methanol-water mixture was conducted in an outer irradiation quartz cell, which was connected to a closed gas circulation system (Fig. S1 in supplemental material). The $\text{Bi}_4\text{Ti}_{3-x}\text{Cr}_x\text{O}_{12}$ nanosheets (0.2 g) were dispersed in deionized water (400 ml) together with methanol (30 ml) in the cell by a magnetic stirrer after sonication (10 min). The reactant

solution was purged with Ar gas for 30 min before reaction in order to eliminate dissolved O_2 . The removal of oxygen from the system prior to hydrogen evolution experiments is necessary to inhibit the backward reaction between H_2 and O_2 . Furthermore, the removal of oxygen from the system can improve the purity of hydrogen and reduce the risk of explosion. Then, the reactor was irradiated using a 300 W Xe lamp for 4 h. A cut-off filter (Changtuo, China) was used to obtain the visible light irradiation ($\lambda > 420 \text{ nm}$). The amount of H_2 evolution was determined using a gas chromatograph (Beijing, GC-3240, TCD, Ar carrier), which was connected to a gas-circulation line. In addition, the amount of H_2 evolution was given as average value of the five parallel samples. For reusability tests, the photocatalytic test over the same $\text{Bi}_4\text{Ti}_{2.6}\text{Cr}_{0.4}\text{O}_{12}$ photocatalyst was repeated three times for hydrogen evolution from methane-water mixture. After each run, the used catalyst was recycled by a process of centrifugation, filtration, washing by DI water and drying at 100 °C for 3 h. In order to check effect of solvent type on photocatalytic H_2 production, ethanol and isopropanol were used at same experimental conditions, respectively.

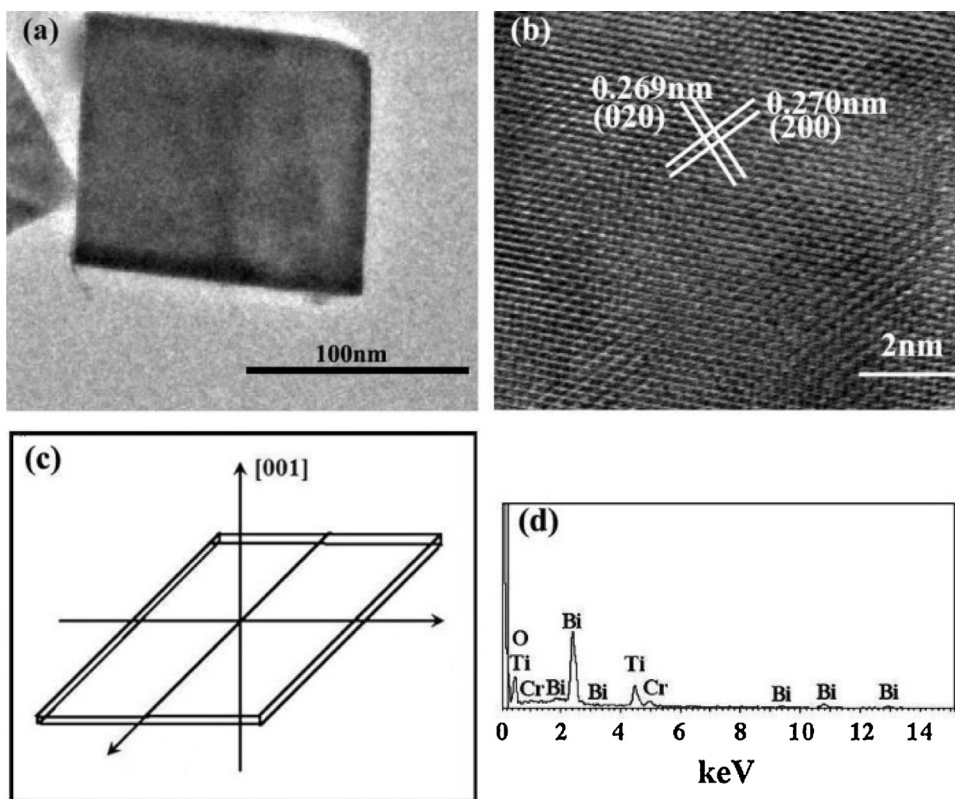


Fig. 2. (a) TEM and (b) HRTEM images of $\text{Bi}_4\text{Ti}_{2.6}\text{Cr}_{0.4}\text{O}_{12}$ nanosheet, (c) Schematic illustration of the crystal orientation of the nanosheet, and (d) EDS pattern of the nanosheets.

The photocatalytic activity of sample was also evaluated by the degradation of methyl orange (MO) in aqueous solution under the irradiation of the 300 W xenon lamp with a 420 nm cut-off filter as the visible light source and a self-made glass vessel with a water-cooling jacket as reactor. The irradiation distance between the lamp and the sample was 15 cm. In a typical experimental process, the photocatalytic reaction was performed on a 50 ml 20 mg/l MO solution mixed with 40 mg photocatalyst in a reactor under magnetic stirring, which was irradiated using the xenon lamp. Before irradiation, the suspension was stirred for 30 min and kept in the dark to ensure an adsorption–desorption equilibrium. The reaction temperature was kept at room temperature by cooling water to prevent any thermal catalytic effect. The degradation efficiency of MO was evaluated by centrifuging the retrieved samples and recording the intensity of absorption peak of MO ($\lambda = 464$ nm) relative to its initial intensity (C/C_0) using a UV–vis spectrophotometer (Model lambda 35, Perkin-Elmer).

3. Results and discussion

3.1. Characterization

The synthesized samples were examined for their morphology and particle size distribution by using SEM. Fig. 1a–e shows the representative SEM images of $\text{Bi}_4\text{Ti}_{3-x}\text{Cr}_x\text{O}_{12}$ ($x = 0–0.5$) particles prepared with sol-gel hydrothermal method. The observation shows that the chromium doping had significant influence on the morphologies of samples. It is interesting that the $\text{Bi}_4\text{Ti}_{3-x}\text{Cr}_x\text{O}_{12}$ particles with $x = 0–0.4$ consisted mostly of regular rectangular shaped nanosheets with uniform size distribution. Their average side length and thickness are listed in Table 1. It is found that the particle size of catalyst became smaller with an increase of Cr content. The decrease in the particle size could be attributed to the increasing oxygen vacancies created by the substitution of Cr

Table 1

The average side length and thickness of various synthesized nanosheets.

Samples	average side length (nm)	average thickness (nm)
$\text{Bi}_4\text{Ti}_3\text{O}_{12}$ nanosheets	245	40
$\text{Bi}_4\text{Ti}_{2.85}\text{Cr}_{0.15}\text{O}_{12}$ nanosheets	210	26
$\text{Bi}_4\text{Ti}_{2.7}\text{Cr}_{0.3}\text{O}_{12}$ nanosheets	156	21
$\text{Bi}_4\text{Ti}_{2.6}\text{Cr}_{0.4}\text{O}_{12}$ nanosheets	95	15

ion for a part of Ti ion sites in the $\text{Bi}_4\text{Ti}_3\text{O}_{12}$ lattice [38]. Notably, $\text{Bi}_4\text{Ti}_{2.6}\text{Cr}_{0.4}\text{O}_{12}$ shows 95 nm of the average side length and 15 nm of the thickness, which are 150 and 25 nm less than those of the sample without Cr, respectively. In contrast, the SEM image of $\text{Bi}_4\text{Ti}_{3-x}\text{Cr}_x\text{O}_{12}$ ($x = 0.5$) indicates a lot of irregularly shaped particles due to significant agglomeration, with ~ 70 nm of diameter size, even though some small nanosheets were observed [Fig. 1e]. The particle agglomeration could be due to destruction of nanosheet structure by excessive adsorbed Cr on the surface of catalysts. These analyses demonstrate that the addition of chromium in appropriate amounts not only maintains the physical feature of perfect nanosheets, but also notably reduces their particle sizes. The small nanosheet size would potentially enhance its photocatalytic performance according to our previous report [36]. For comparison, the SEM image of calcined $\text{Bi}_4\text{Ti}_3\text{O}_{12}$ particles at 850°C was also examined, as shown in Fig. 1f. The calcined sample displays significantly larger aggregated particles with much more irregular shape and the diameter of about 1.6–3.2 μm , agreeing with the previous report [39].

To further see microstructure, TEM analysis of the $\text{Bi}_4\text{Ti}_{2.6}\text{Cr}_{0.4}\text{O}_{12}$ nanostructure was performed. The TEM image in Fig. 2a reveals that the side length of an individual nanosheet was about 100–120 nm, consistent with the SEM results. Fig. 2b shows the HRTEM image of a representative $\text{Bi}_4\text{Ti}_{2.6}\text{Cr}_{0.4}\text{O}_{12}$ nanosheet. The interplanar spacings for the two selected sets of marked

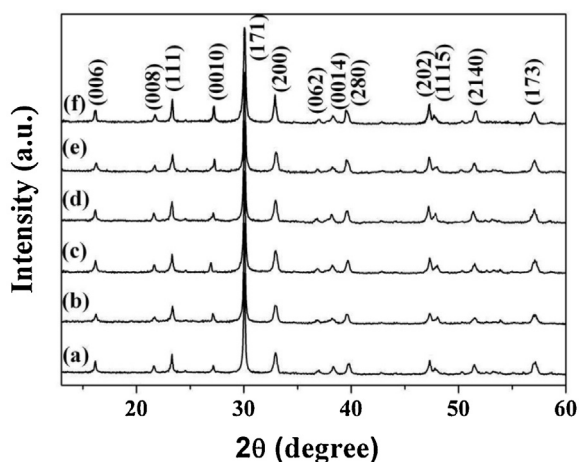


Fig. 3. XRD patterns of $\text{Bi}_4\text{Ti}_{3-x}\text{Cr}_x\text{O}_{12}$ ($x=0-0.5$) nanosheets (a) $x=0.0$, (b) $x=0.15$, (c) $x=0.30$, (d) $x=0.40$, (e) $x=0.50$, and (f) calcined $\text{Bi}_4\text{Ti}_3\text{O}_{12}$ sample.

adjacent lattices were 0.269 nm and 0.270 nm, corresponding to (020) and (200) atomic planes of $\text{Bi}_4\text{Ti}_{2.6}\text{Cr}_{0.4}\text{O}_{12}$, respectively [40]. Based on these results, it could be concluded that the in-plane surfaces of rectangular shaped nanosheets lie on (001) plane, as schematically illustrated in Fig. 2c. To examine the chemical components of the $\text{Bi}_4\text{Ti}_{3-x}\text{Cr}_x\text{O}_{12}$ nanosheets, EDS was performed. Fig. 2d shows the EDS pattern of the $\text{Bi}_4\text{Ti}_{2.6}\text{Cr}_{0.4}\text{O}_{12}$ nanosheets prepared. The analysis shows that four elements of Bi, Ti, Cr, and O appear, and their atomic ratio was 21.25: 13.58: 2.21: 62.96, which matches the calculated elemental ratio based on $\text{Bi}_4\text{Ti}_{2.6}\text{Cr}_{0.4}\text{O}_{12}$. Combined with the analysis results of Cr content by inductively coupled plasma-atomic emission spectroscopy (Table S1), it can be further demonstrated that the pure $\text{Bi}_4\text{Ti}_{2.6}\text{Cr}_{0.4}\text{O}_{12}$ was synthesized successfully.

XRD was performed to examine the phase identity of the synthesized photocatalysts and to support the above SEM and TEM findings. Fig. 3 shows the XRD patterns of hydrothermally synthesized and conventionally calcined samples. As shown in Fig. 3a, all diffraction peaks of the hydrothermally synthesized $\text{Bi}_4\text{Ti}_{3-x}\text{Cr}_x\text{O}_{12}$ ($x=0-0.5$) can be well indexed to $\text{Bi}_4\text{Ti}_3\text{O}_{12}$ with a space group $Fm\bar{3}m$ and an orthorhombic structure (JCPDS No. 73-2181). No additional characteristic peaks were observed, indicating that the photocatalysts were single crystalline oxide. The sharp diffraction peaks suggest that the single-phase samples have good crystallinity. The analysis demonstrates the signature of the $\text{Bi}_4\text{Ti}_3\text{O}_{12}$ phase was well maintained with Cr addition, implying that the Cr is most likely introduced as a substitute within the perovskite structure. Bi^{3+} is at the position of A site in the perovskite structure. Compared with the ionic radius of Bi^{3+} (0.103 nm), the ionic radius of Cr^{3+} (0.062 nm) is closer to that of Ti^{4+} ion (0.074 nm). Thus, the chromium ions should substitute for titanium ions in the bulk, which occupy B sites in the perovskite structures [35]. Interestingly, a close examination in the vicinity of 2θ around $29.5-30.5^\circ$ indicates that the peak positions slightly shifted to higher angles with the increase in the amounts of doped chromium (Fig. S2), suggesting that a part of chromium at least is incorporated into the $\text{Bi}_4\text{Ti}_3\text{O}_{12}$ lattice. In addition, the features of these XRD patterns were also similar to that of the $\text{Bi}_4\text{Ti}_3\text{O}_{12}$ calcined at 850°C (Fig. 3f). However, the synthesized temperature (200°C) for the $\text{Bi}_4\text{Ti}_{3-x}\text{Cr}_x\text{O}_{12}$ nanosheets with the present sol-gel hydrothermal process is much lower than that (850°C) required for the $\text{Bi}_4\text{Ti}_3\text{O}_{12}$ with conventional solid-state reaction technique.

XPS was performed to study the chemical composition and bonding states of the $\text{Bi}_4\text{Ti}_{2.6}\text{Cr}_{0.4}\text{O}_{12}$ nanosheet surface. Fig. 4a clearly indicates that all of the peaks on the XPS survey spectra

could be attributed to Bi, Ti, Cr, O and C core levels, and no additional peaks were observed. The presence of the C peak primarily results from carbon tape used for the XPS measurement. Fig. 4b–e shows the high resolution XPS spectra of the Cr 2p, Ti 2p, Bi 4f, and O 1s core levels and their Gaussian-resolved results, respectively. The Gaussian-resolved result for Cr 2p spectrum in Fig. 4b displays the peak at around 576.23 eV, which could be attributed to trivalent chromium (Cr^{3+}), a low oxidation state, according to the literature [41]. The two main peaks at 457.59 and 465.42 eV in Fig. 4c could be ascribed to Ti 2p $3/2$ and Ti 2p $1/2$ states respectively, which are in good agreement with those of pure TiO_2 [42]. The Gaussian-resolved result for the Bi 4f spectrum of the $\text{Bi}_4\text{Ti}_{2.6}\text{Cr}_{0.4}\text{O}_{12}$ nanosheets in Fig. 4d shows two main peaks centered at 159.21 eV and 164.42 eV, which were assigned to Bi 4f $7/2$ and Bi 4f $5/2$, respectively. The assignment is consistent with the reference [43]. The Bi 4f doublet display the chemical shift of about 2.2–2.4 eV as compared to those of metallic Bi where the binding energy locations of its 4f $7/2$ and 4f $5/2$ core levels are at 156.8 and 162.2 eV, respectively [44]. The shift value is less than the typical value of 3.1 eV between Bi_2O_3 and metallic Bi [45]. The observed shift suggests the existence of bismuth with the valence state less than $3+$ ($\text{Bi}(+3-x)$). Generation of the Bi species could be understood due to the oxygen deficiency and enhanced concentration of oxygen vacancies in the vicinity of bismuth cations, either in the perovskite lattice structure or in the Bi_2O_3 layer. Fig. 4e indicates that the high-resolution XPS spectrum of O 1s was wide and asymmetric, implying that there exists more than one chemical state in the oxygen species of the nanosheet surface. The deconvolution of the O 1s spectrum shows contributions from two oxygen species, i.e. the lattice oxygen (O^{2-} in the stronger Ti–O bond) at the lower binding energy of 530.13 eV and the surface adsorbed oxygen ($-\text{OH}$ group and chemisorbed oxygen-containing species) at a higher bonding energy of 532.33 eV [45].

In addition, the Ti 2p, Bi 4f and O 1s XPS of $\text{Bi}_4\text{Ti}_3\text{O}_{12}$ and $\text{Bi}_4\text{Ti}_{2.6}\text{Cr}_{0.4}\text{O}_{12}$ nanosheets were compared in order to study the Cr modification on photocatalyst surface, as shown in Fig. S3. Clearly, $\text{Bi}_4\text{Ti}_{2.6}\text{Cr}_{0.4}\text{O}_{12}$ shows lower binding energy of Ti 2p XPS than $\text{Bi}_4\text{Ti}_3\text{O}_{12}$ (Fig. S3b). Similar shifts of binding energy in Bi 4f and O 1s XPS of $\text{Bi}_4\text{Ti}_{2.6}\text{Cr}_{0.4}\text{O}_{12}$ were also observed as compared with those of $\text{Bi}_4\text{Ti}_3\text{O}_{12}$ (Fig. S3c–d). The XPS observations further confirm incorporation of Cr into the surface structure of $\text{Bi}_4\text{Ti}_3\text{O}_{12}$ nanosheets.

3.2. Photocatalytic performance

3.2.1. Hydrogen evolution from alcohol-water mixture

Photocatalytic reduction of H_2O into H_2 over catalyst in a methanol-water solution was performed using a quartz cell reactor. Methanol was used as a scavenger for holes. The activities of the prepared photocatalysts under visible-light illumination are shown in Fig. 5. The hydrothermally synthesized $\text{Bi}_4\text{Ti}_3\text{O}_{12}$ photocatalyst displays the H_2 evolution rate of around $41 \mu\text{mol g}^{-1} \text{h}^{-1}$, more than that of calcined Cr-free sample ($35 \mu\text{mol g}^{-1} \text{h}^{-1}$). This demonstrates superiority of the present hydrothermal synthesis over conventional calcination preparation for visible-light-driven $\text{Bi}_4\text{Ti}_3\text{O}_{12}$ photocatalyst. Interestingly, addition of Cr to $\text{Bi}_4\text{Ti}_3\text{O}_{12}$ nanosheets improves photocatalytic generation of hydrogen. With an increase of introduced Cr amount, H_2 evolution rate of photocatalyst progressively increased, with $\text{Bi}_4\text{Ti}_{2.6}\text{Cr}_{0.4}\text{O}_{12}$ reaching maximum of $117 \mu\text{mol g}^{-1} \text{h}^{-1}$. The rate value is ~ 2.85 times higher than that of Cr-free nanosheets, and also much higher than that of the particles reported in the reference [35]. On the other hand, any further increase in the Cr content resulted in deteriorated performance of the photocatalyst and a decrease in the hydrogen evolution rate, though this rate was still higher than Cr-free nanosheet photocatalyst. The decrease in hydrogen evolution rate

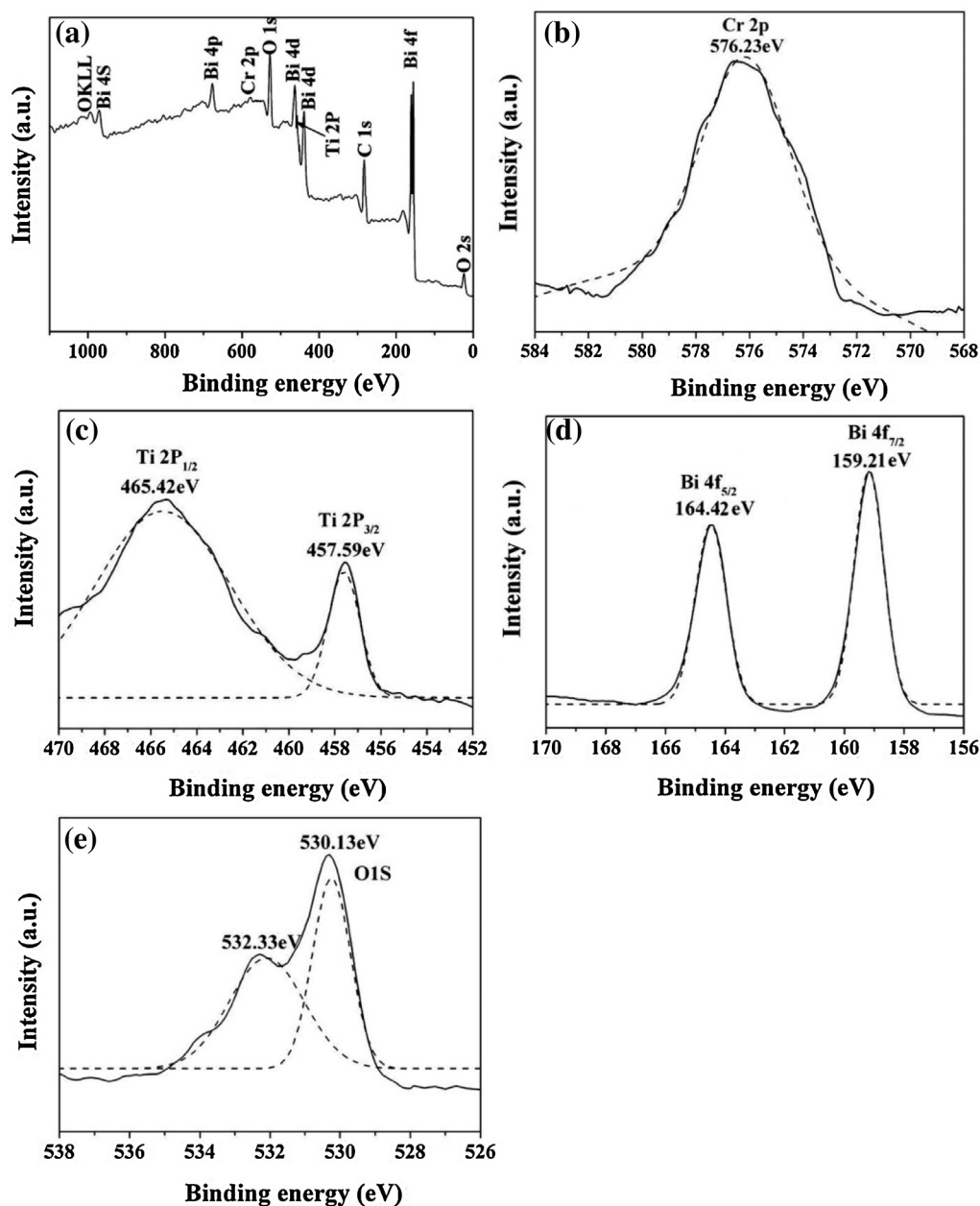


Fig. 4. XPS spectra of the as-prepared $\text{Bi}_4\text{Ti}_{2.6}\text{Cr}_{0.4}\text{O}_{12}$ nanosheets: (a) a typical XPS survey spectrum, and high-resolution XPS spectra of (b) Cr 2p, (c) Ti 2p, (d) Bi 4f, and (e) O1s.

with the excessive Cr content could be attributed to the significant particle agglomeration, which results in the decreased active surface sites and exposed {010} facet, and the increase in the charge recombination sites as discussed below. Moreover, without methanol as a sacrificial agent, the $\text{Bi}_4\text{Ti}_{2.6}\text{Cr}_{0.4}\text{O}_{12}$ nanosheets still show photocatalytic activity, causing hydrogen evolution from pure water though the hydrogen production rate is low (Fig. S4).

3.2.2. Photocatalytic mechanism of methanol-assisted hydrogen evolution

It has been demonstrated that methanol is an ideal organic sacrificial agent in water splitting reactions [46–48]. Without methanol as a sacrificial agent, the initial hole-generated hydroxyl radicals and protons are prone to recombination to form water and very little hydrogen is released. In this study, the hydrogen evolution from pure water is confirmed above even though it is in low efficiency. For the H_2 evolution from a methanol-water solution, when

$\text{Bi}_4\text{Ti}_{3-x}\text{Cr}_x\text{O}_{12}$ photocatalysts absorb visible light from illumination source, electrons in the valence band of the $\text{Bi}_4\text{Ti}_{3-x}\text{Cr}_x\text{O}_{12}$ become excited and promoted to the conduction band, which thus creates the negative electron (e^-) and positive hole (h^+) pair (see, Eq. (1)). The hole reacts with H_2O molecule (adsorbed state) to form H^+ and $\cdot\text{OH}$ radicals (see, Eq. (2)). Subsequently, the $\cdot\text{OH}$ is consumed to form $\cdot\text{CH}_2\text{OH}$ and H_2O through the chemical reaction with methanol (CH_3OH) (see, Eq. (3)). The methanol radical breaks down to form formaldehyde, proton and electron, as shown in Eq. (4). The produced proton is reduced to hydrogen (Eq. (5)). Meanwhile, the formaldehyde further oxidizes to formic acid and releases hydrogen gas (Eq. (6)). The formic acid finally oxidizes to carbon dioxide and hydrogen gas (Eq. (7)). The overall reaction can be expressed in Eq. (8). The plausible reaction pathways of H_2 production from methanol-water mixture were as following [49,50]:



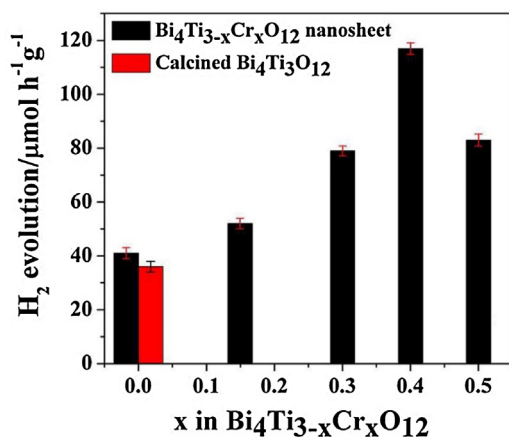


Fig. 5. The hydrogen evolution of Bi₄Ti_{3-x}Cr_xO₁₂ nanosheets, calcined Bi₄Ti₃O₁₂ and P25 in the methanol aqueous solution under visible light irradiation ($\lambda > 420$ nm).

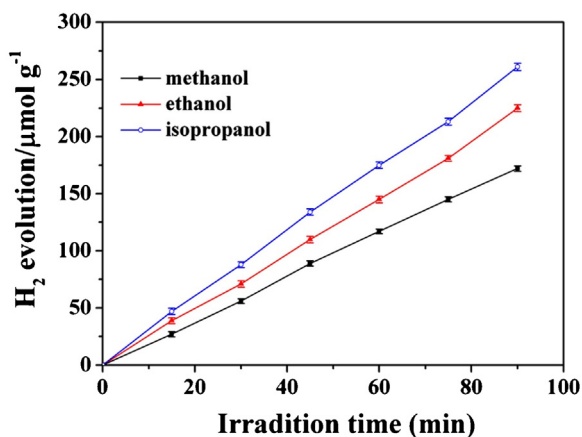
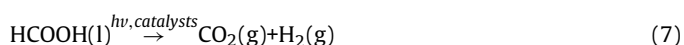
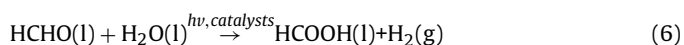
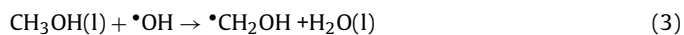
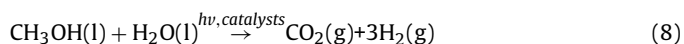


Fig. 6. Effect of solvent composition on hydrogen production over Bi₄Ti_{2.6}Cr_{0.4}O₁₂ nanosheets under visible-light irradiation ($\lambda > 420$ nm).



Overall:



3.2.3. Effect of solvent type on photocatalytic H₂ evolution

The influences of solvent type on photocatalytic H₂ evolution were investigated. Fig. 6 shows the relative effects of different alcohol–water mixtures on H₂ evolution over Bi₄Ti_{2.6}Cr_{0.4}O₁₂ photocatalyst under visible light ($\lambda > 420$ nm). The isopropanol, ethanol, and methanol aqueous solution were used in the photocatalytic reaction. As shown in Fig. 6, the order of the photocatalytic H₂ evolution rate was isopropanol > ethanol > methanol. The rate order could be related to the thickness of the electrical double layer (EDL) formed between catalyst surface and alcohol–water solution. Alcohols (such as isopropanol, ethanol, or methanol) in addition to pure water are regarded as crucial electron donors for photocatalytic H₂ generation since little H₂ would be produced without

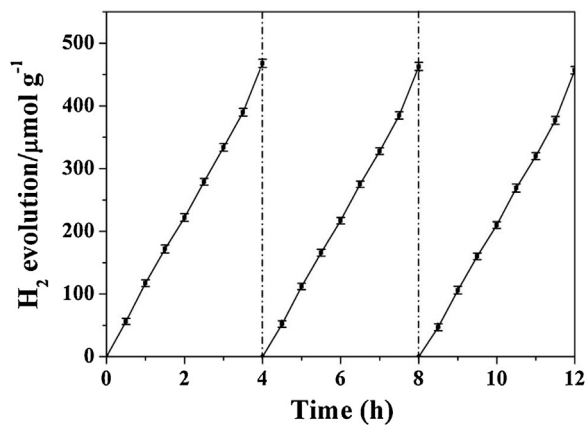


Fig. 7. Stability study of hydrogen evolution over Bi₄Ti_{2.6}Cr_{0.4}O₁₂ nanosheets under visible-light irradiation.

added electron donors even under UV light irradiation [50]. The thinner the EDL is, the more efficiently holes are trapped by the electron donors, which would increase H₂ evolution rate. The EDL thickness (k) could be estimated by the Debye equation:

$$k = \left(\frac{2F^2\mu}{\varepsilon\varepsilon_0RT} \right)^{0.5} \quad (9)$$

where ε is the dielectric constant of the solvent or mixed solvent system, ε_0 is the permittivity of free space (8.854×10^{-12} C²J⁻¹m⁻¹), μ is the ionic strength of the background electrolyte (mol m⁻³), R is the gas constant (8.314 J mol⁻¹ K⁻¹), T is temperature in units of K, and F is the Faraday constant (96485 C mol⁻¹). Clearly, the k value is inversely proportional to the ε value. The ε values of isopropanol, ethanol, methanol and water are 18.3, 24.6, 32.7 and 80.4, respectively [51,52]. Therefore, the EDL thickness (k) of alcohol–water solution would decrease when alcohols are added to the water, and the decreased order of the k value is: isopropanol–water solution > ethanol–water solution > methanol–water solution, which is the same as their H₂ evolution rate order. The observation agrees with the previous report [53]. This explains the difference of H₂ evolution rate from different alcohol–water solutions.

3.2.4. Reusability of photocatalyst in the hydrogen evolution

In order to investigate the reusability and stability of the synthesized photocatalyst, a cycling experiment was performed with the optimal Bi₄Ti_{2.6}Cr_{0.4}O₁₂ under continuous visible-light illumination. The cycling experiment was repeated three times, and the results are shown in Fig. 7. The first run showed around 467 μmol g⁻¹ of the cumulative hydrogen evolution during test time of 4 h. As compared to the first run, the second run only indicated the decrease of ~2% in the hydrogen evolution rate. Particularly, the third run almost remained the same H₂ evolution rate as that in the second run. These observations confirm the excellent reusability of the photocatalyst.

3.2.5. Photocatalytic MO degradation

The photocatalytic activity of Bi₄Ti_{2.6}Cr_{0.4}O₁₂ nanosheets was also investigated by degrading MO aqueous solution under visible light irradiation. As shown in Fig. 8, the blank tests without any added catalyst showed no obvious C/C₀ change in the testing period of 240 min, demonstrating no MO degradation occurs. The photodegradation of MO in the presence of P25 and calcined Bi₄Ti₃O₁₂ was relatively slow, with 22 and 36% respectively of MO degraded during the whole illumination period. In contrast, hydrothermally synthesized Bi₄Ti₃O₁₂ nanosheets show enhanced

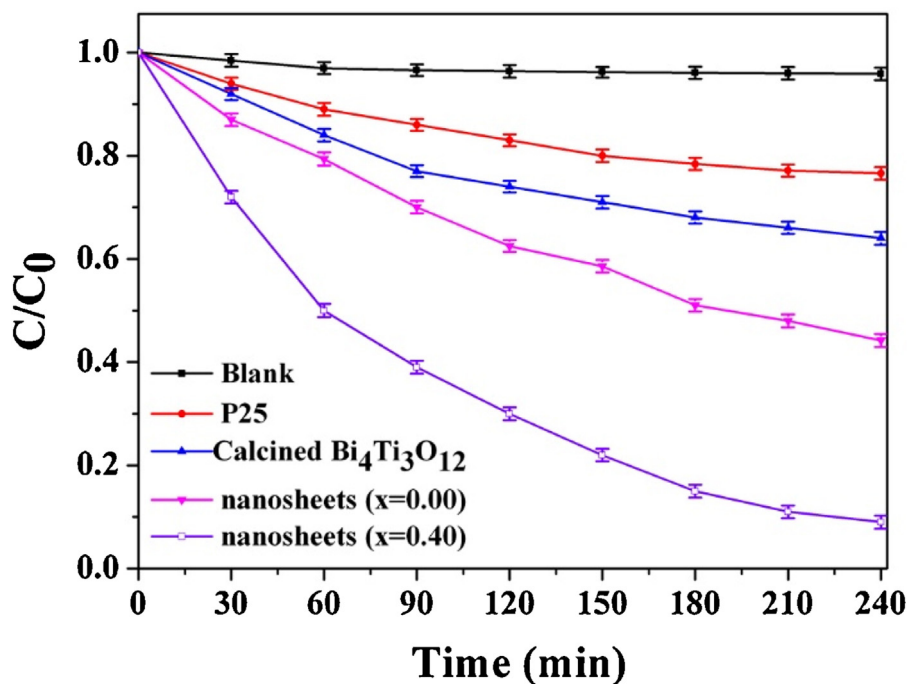


Fig. 8. The photodegradation efficiencies of MO as a function of irradiation time with various samples under visible-light ($\lambda > 420$ nm) irradiation.

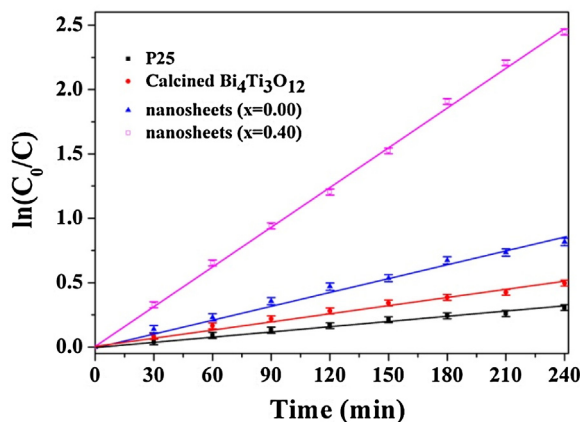


Fig. 9. Kinetic linear simulation curves of photocatalytic degradation of MO over various samples.

activity, with 55% of MO photodegradation. Remarkably, in the presence of $\text{Bi}_4\text{Ti}_{2.6}\text{Cr}_{0.4}\text{O}_{12}$ nanosheets, the photodegradation of MO was much faster, with conversions up to 91% during the whole illumination period. The photodegradation kinetics were fitted to a pseudo-first-order reaction, $\ln(C_0/C) = kt$, where k is the apparent rate constant (Fig. 9). The $\text{Bi}_4\text{Ti}_{2.6}\text{Cr}_{0.4}\text{O}_{12}$ photocatalyst showed the highest average apparent rate constant of 0.01003 min^{-1} , about 3-fold higher than that of the $\text{Bi}_4\text{Ti}_3\text{O}_{12}$ nanosheet (0.00341 min^{-1}). The average apparent rate constants for calcined $\text{Bi}_4\text{Ti}_3\text{O}_{12}$ and P25 were only 0.00186 and 0.00111 min^{-1} , respectively.

3.3. Insights into the photocatalytic performance of the Cr-modified $\text{Bi}_4\text{Ti}_3\text{O}_{12}$

3.3.1. UV-visible analysis

In order to obtain an insight into the optical characteristics of the synthesized photocatalysts, the UV-visible absorption spectra of these materials was examined, as shown in Fig. 10. Firstly, As shown in Fig. 10a, Cr-free $\text{Bi}_4\text{Ti}_3\text{O}_{12}$ nanosheets indicate much

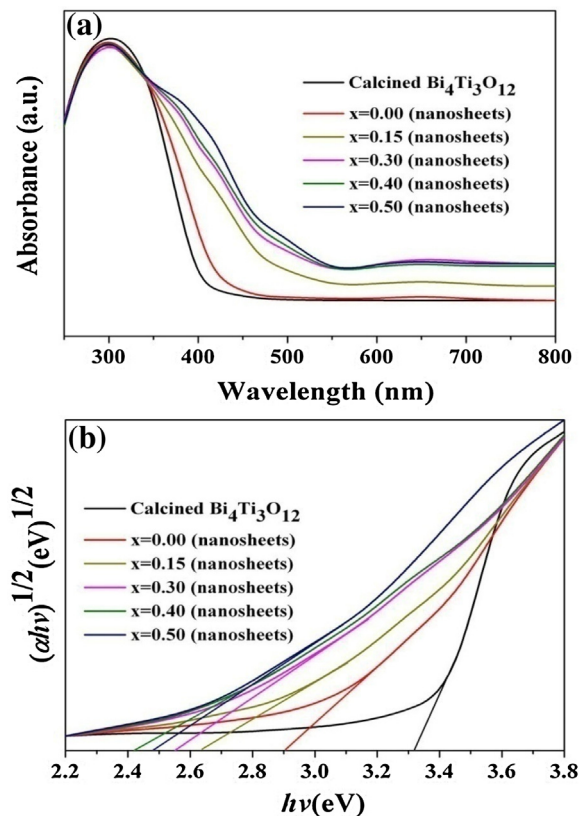


Fig. 10. (a) UV-vis absorption spectrum of the as-prepared $\text{Bi}_4\text{Ti}_{3-x}\text{Cr}_x\text{O}_{12}$ ($x = 0-0.5$) nanosheets and calcined $\text{Bi}_4\text{Ti}_3\text{O}_{12}$. (b) The plot of $(ah\nu)^{1/2}$ as a function of photon energy ($h\nu$).

stronger absorption in the wavelength range of 350–500 nm as compared to calcined $\text{Bi}_4\text{Ti}_3\text{O}_{12}$ particles. The absorption difference could be contributed to the different crystal growth modes of the two samples, as described in our previous report [36].

Secondly, compared to Cr-free $\text{Bi}_4\text{Ti}_3\text{O}_{12}$ nanosheets, $\text{Bi}_4\text{Ti}_{2.85}\text{Cr}_{0.15}\text{O}_{12}$ nanosheets indicated a red shift in the absorption edge by 120 nm. With an increase of the Cr content in the synthesized products there is a progressive red shift in the absorption edges. According to previous density functional theory (DFT) calculation, the conduction bands (CB) of $\text{Bi}_4\text{Ti}_3\text{O}_{12}$ are mainly attributable to the Ti 3d + Bi 6p orbitals, and the valence bands (VB) are composed of O 2p + Bi 6s hybrid orbitals. However, the CB of chromium-modified $\text{Bi}_4\text{Ti}_3\text{O}_{12}$ are mainly attributable to the Ti 3d + Bi 2p + Cr 3d orbitals, and the O 2p + Cr 3d hybrid orbitals are the main contribution to the VB [35]. The contribution of the Cr 3d electrons to above the VB and the CB facilitates efficient electron transit from the impurity level, thus leading to the red shift of the absorption band edge of the Cr-modified $\text{Bi}_4\text{Ti}_3\text{O}_{12}$ nanosheets.

The band gap values could be obtained from the UV–vis absorption spectra, using the following equation [54]:

$$\alpha h\nu = A(h\nu - E_g)^{n/2} \quad (10)$$

where α , h , ν , E_g , and A are absorption coefficient, Planck's constant, light frequency, band gap, and a constant, respectively. In the case that the fundamental absorption of $\text{Bi}_4\text{Ti}_3\text{O}_{12}$ possesses an indirect transition between bands, then n equals 4 [55]. The band gap values, as estimated from the $(\alpha h\nu)^{1/2}$ versus $h\nu$ plot by extrapolating its tangent line to the energy axis at $\alpha = 0$, are 3.31, 2.90, 2.63, 2.55, 2.42 and 2.48 eV for calcined $\text{Bi}_4\text{Ti}_3\text{O}_{12}$, hydrothermally formed $\text{Bi}_4\text{Ti}_3\text{O}_{12}$, $\text{Bi}_4\text{Ti}_{2.85}\text{Cr}_{0.15}\text{O}_{12}$, $\text{Bi}_4\text{Ti}_{2.7}\text{Cr}_{0.3}\text{O}_{12}$, $\text{Bi}_4\text{Ti}_{2.6}\text{Cr}_{0.4}\text{O}_{12}$, and $\text{Bi}_4\text{Ti}_{2.5}\text{Cr}_{0.5}\text{O}_{12}$, respectively (Fig. 10b). Obviously, compared to calcined sample, $\text{Bi}_4\text{Ti}_3\text{O}_{12}$ nanosheets shows significantly decreased band gap value. The decrease of the band gap value could be due to nanosheet morphology and reduced particle size [54]. The value consecutively decreased with an increase of Cr content, then reached the minimum for $\text{Bi}_4\text{Ti}_{2.6}\text{Cr}_{0.4}\text{O}_{12}$, and finally increased a little with further increase in the Cr content. Although the absorbance measurements indicate that a combined absorption of UV–vis light occurs for all photocatalysts, addition of varying Cr content significantly extends photoabsorption of catalyst to the visible light region. Specifically, the $\text{Bi}_4\text{Ti}_{2.6}\text{Cr}_{0.4}\text{O}_{12}$ nanosheet shows the strongest photoabsorption in the visible light region, which could produce photoexcited charges primarily responsible for its highest photocatalytic activities in the both H_2 evolution and MO degradation under visible light irradiation. Such benefits have also been observed in the Mn-modified $\text{Bi}_2\text{Ti}_2\text{O}_7$ photocatalyst for H_2 evolution from methanol–water mixture [56].

3.3.2. PL analysis

PL measurements were performed to observe the effect of Cr modification on the electron–hole recombination in the $\text{Bi}_4\text{Ti}_3\text{O}_{12}$. As shown in Fig. 11, when excited by the light at $\lambda = 320$ nm, all samples indicate two characteristic PL emission peaks at around 412 and 461 nm, as ascribed to the recombination of photoexcited electrons and holes [57]. As compared to the calcined $\text{Bi}_4\text{Ti}_3\text{O}_{12}$ particles, the $\text{Bi}_4\text{Ti}_3\text{O}_{12}$ nanosheets shows an obvious decrease in the PL intensity. This is because the excited electrons are delocalized in the $\text{Bi}_4\text{Ti}_3\text{O}_{12}$ nanosheets and are not consumed by recombination. It is interesting that addition of Cr to $\text{Bi}_4\text{Ti}_3\text{O}_{12}$ nanosheets indicates further decrease in the PL intensity, suggesting that an efficiently reduced recombination of electron–hole pairs occurs in the presence of Cr. With an increase in the Cr amount, the PL intensity decreases in the order: $\text{Bi}_4\text{Ti}_3\text{O}_{12} > \text{Bi}_4\text{Ti}_{2.85}\text{Cr}_{0.15}\text{O}_{12} > \text{Bi}_4\text{Ti}_{2.7}\text{Cr}_{0.3}\text{O}_{12} > \text{Bi}_4\text{Ti}_{2.5}\text{Cr}_{0.5}\text{O}_{12} > \text{Bi}_4\text{Ti}_{2.6}\text{Cr}_{0.4}\text{O}_{12}$. In order to correlate PL intensity with catalytic activity, hydrogen evolution from methanol–water system under UV light condition was performed over $\text{Bi}_4\text{Ti}_3\text{O}_{12}$ and $\text{Bi}_4\text{Ti}_{2.6}\text{Cr}_{0.4}\text{O}_{12}$ nanosheets (Fig. S5). The Cr-modified nanosheets with low PL intensity show much higher hydrogen evolution rate than Cr-free ones, which display high PL intensity. Therefore, it is

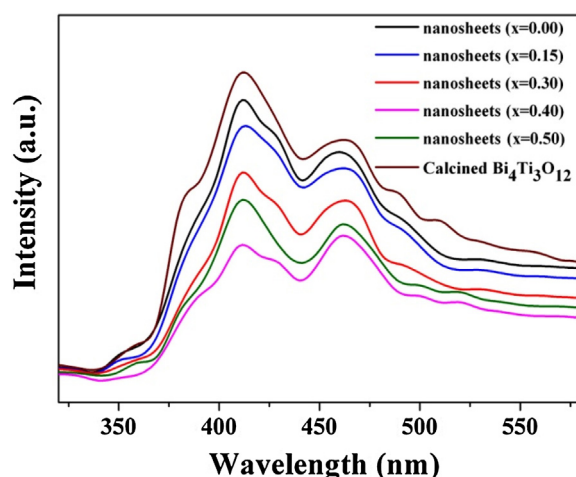


Fig. 11. Photoluminescence (PL) spectra of $\text{Bi}_4\text{Ti}_{3-x}\text{Cr}_x\text{O}_{12}$ ($x = 0–0.5$) nanosheets and calcined $\text{Bi}_4\text{Ti}_3\text{O}_{12}$ excited at the wavelength of 320 nm.

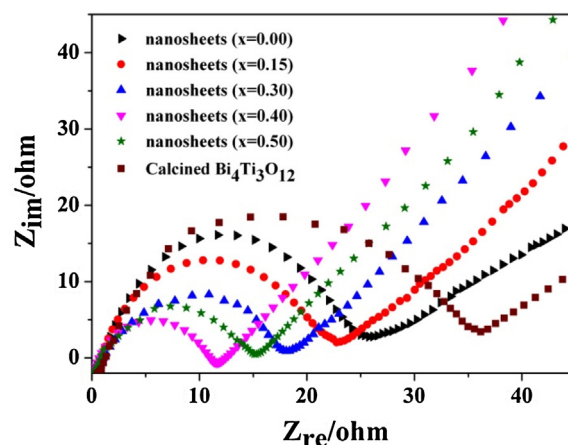


Fig. 12. Nyquist plots for the photoelectrodes of $\text{Bi}_4\text{Ti}_{3-x}\text{Cr}_x\text{O}_{12}$ ($x = 0–0.5$) nanosheets and calcined $\text{Bi}_4\text{Ti}_3\text{O}_{12}$ in 0.1 M KCl and 0.1 M $\text{K}_3[\text{Fe}(\text{CN})_6]/\text{K}_4[\text{Fe}(\text{CN})_6]$ (1:1) solution at pH = 7 under visible-light irradiation ($\lambda > 420$ nm).

reasonable to deduce that the decrease order in the PL intensity is consistent with the increased activity order of photocatalysts in the visible-light. The finding drawn from PL measurements complements that from EIS analysis (discussed below).

3.3.3. Electrochemical impedance analysis

EIS was employed to evaluate the electron-transfer capacity of the synthesized photocatalysts, as shown in Fig. 12. The diagram of each sample includes a semicircular part, which reflects the charge transfer process, and a linear part with a slope of 45° belonged to the diffusion-controlled step [58]. The electron-transfer resistance (R_{ct}), whose value is acquired by measuring the semicircle's diameter, reflects the effectiveness of charge transfer occurring in the system. In summary, the smaller R_{ct} value is, the more effective the charge transfer within the system is [59,60]. Table 2 lists the R_{ct} values of samples from the EIS, and shows that there is a decreased R_{ct} value in the nanosheet catalyst as compared to the calcined sample. Remarkably, among all catalysts $\text{Bi}_4\text{Ti}_{2.6}\text{Cr}_{0.4}\text{O}_{12}$ displays the smallest R_{ct} value, implying the best separation efficiency of photogenerated charges. Overall, the decreasing order in the R_{ct} value is $\text{Bi}_4\text{Ti}_3\text{O}_{12} > \text{Bi}_4\text{Ti}_{2.85}\text{Cr}_{0.15}\text{O}_{12} > \text{Bi}_4\text{Ti}_{2.7}\text{Cr}_{0.3}\text{O}_{12} > \text{Bi}_4\text{Ti}_{2.5}\text{Cr}_{0.5}\text{O}_{12} > \text{Bi}_4\text{Ti}_{2.6}\text{Cr}_{0.4}\text{O}_{12}$, coinciding with the increased activity order of photocatalysts.

Table 2
The R_{ct} values of various samples.

Samples	R_{ct} (Ω)
calcined $\text{Bi}_4\text{Ti}_3\text{O}_{12}$	36.1
$\text{Bi}_4\text{Ti}_3\text{O}_{12}$ nanosheets	25.7
$\text{Bi}_4\text{Ti}_{2.85}\text{Cr}_{0.15}\text{O}_{12}$ nanosheets	22.9
$\text{Bi}_4\text{Ti}_{2.7}\text{Cr}_{0.3}\text{O}_{12}$ nanosheets	18.1
$\text{Bi}_4\text{Ti}_{2.6}\text{Cr}_{0.4}\text{O}_{12}$ nanosheets	11.7
$\text{Bi}_4\text{Ti}_{2.5}\text{Cr}_{0.5}\text{O}_{12}$ nanosheets	15.2

The above SEM and TEM results confirm that addition of an optimal Cr content to $\text{Bi}_4\text{Ti}_3\text{O}_{12}$ effectively not only causes diminished particle size but also maintains uniform distribution of thinned nanosheets. The smaller particle size offers more available active reaction sites and the shorter charge transport distance from bulk of nanosheet to reaction surface [61,62]. The short distance ensures low recombination rate or high separation efficiency for photogenerated electron/hole pairs. The thin nanosized sheets with primary exposed {001} facets are believed to reduce the recombination of photogenerated charge carriers or to boost their separation and transfer due to the self-induced internal electric fields in the nanosheets [63]. An excessive Cr content in the $\text{Bi}_4\text{Ti}_{2.5}\text{Cr}_{0.5}\text{O}_{12}$ causes particle agglomeration and leads to decreased surface reaction sites and exposed {001} facets as compared to those in the $\text{Bi}_4\text{Ti}_{2.6}\text{Cr}_{0.4}\text{O}_{12}$, but the catalyst with the highest Cr content still shows more efficient charge separation capacity than the $\text{Bi}_4\text{Ti}_3\text{O}_{12}$ nanosheet. The role of Cr in reducing the recombination of photogenerated electron-hole pairs or improving their separation is thus evident, and this reduced recombination or improved separation was the basis for the observed enhancement in the photocatalytic activities of the Cr-modified nanosheets for visible-light-driven hydrogen evolution and MO degradation. The role of metal ion additives in reducing recombination of electron-hole pair and in enhancing photoreactivity of oxide catalyst has been well documented. For example, Bahnemann and co-workers report that Fe-modified TiO_2 particles show much higher activity for the photodegradation of dichloroacetic acid than pure TiO_2 colloids due to the inhibiting effect of ferric ions within the TiO_2 matrix on the recombination of photogenerated charge carriers [64,65]. Borgarello et al. also demonstrate that additive Cr plays a similar role in the enhanced photoreactivity over the Cr-modified TiO_2 catalyst for water cleavage [66].

4. Conclusions

A series of $\text{Bi}_4\text{Ti}_{3-x}\text{Cr}_x\text{O}_{12}$ ($x=0-0.5$) photocatalysts has been developed via a sol-gel hydrothermal process without the use of any template or organic surfactant. Varying Cr content was successfully added to the orthorhombic structure of $\text{Bi}_4\text{Ti}_3\text{O}_{12}$, and the Cr-modified $\text{Bi}_4\text{Ti}_3\text{O}_{12}$ indicates a significant extension of photoabsorption into the visible light region and a decreased recombination of photogenerated charges as compared to Cr-free $\text{Bi}_4\text{Ti}_3\text{O}_{12}$. An increase in the Cr content considerably improves performance of photocatalysts, and $\text{Bi}_4\text{Ti}_{2.6}\text{Cr}_{0.4}\text{O}_{12}$ shows the highest $117 \mu\text{mol g}^{-1} \text{h}^{-1}$ of the hydrogen evolution rate and ~91% of MO degradation under visible light irradiation, which are 2.85 and 1.65 times those of $\text{Bi}_4\text{Ti}_3\text{O}_{12}$ nanosheet, respectively. Higher Cr concentrations in the $\text{Bi}_4\text{Ti}_{2.5}\text{Cr}_{0.5}\text{O}_{12}$, as compared to $\text{Bi}_4\text{Ti}_{2.6}\text{Cr}_{0.4}\text{O}_{12}$, could act as a trapping center for photogenerated charges and thus, reduce the photocatalytic activity. However, $\text{Bi}_4\text{Ti}_{2.5}\text{Cr}_{0.5}\text{O}_{12}$ still shows about twice the hydrogen evolution rate of $\text{Bi}_4\text{Ti}_3\text{O}_{12}$ nanosheet. The improved photocatalytic performance of the Cr-modified $\text{Bi}_4\text{Ti}_3\text{O}_{12}$, as compared with that of the Cr-free one, is due to its stronger photoabsorption in the visible light region, reduced particle size, unique nanosheet shape, exposed {001} facets and the decreased recombination of photoinduced charge

carriers, or their improved separation. Various alcohol-water mixtures also affect the hydrogen evolution rate of photocatalyst, with the rate order: isopropanol > ethanol > methanol. The high activity and stable reusability of $\text{Bi}_4\text{Ti}_{2.6}\text{Cr}_{0.4}\text{O}_{12}$ suggests that it could be a promising commercial photocatalyst applied to both visible-light-driven hydrogen evolution and organic pollutant degradation.

Acknowledgements

Financial supports from National Natural Science Foundation of China (No. 50702022), the Fundamental Research Funds for the Central Universities, SCUT (No. 2015ZZ012) and Natural Science Foundation of Guangdong Province (No. 2014A030313245) are greatly appreciated.

Appendix A. Supplementary data

Supplementary data associated with this article can be found, in the online version, at <http://dx.doi.org/10.1016/j.apcatb.2016.06.036>.

References

- [1] S. Tanigawa, H. Irie, Appl. Catal. B 180 (2016) 1–5.
- [2] E. Kowalska, K. Yoshiiri, Z. Wei, S. Zheng, E. Kastl, H. Remitat, B. Ohtani, S. Rau, Appl. Catal. B 178 (2015) 133–143.
- [3] G. Kim, S.-H. Lee, W. Choi, Appl. Catal. B 162 (2015) 463–469.
- [4] Y.L. Pang, A.Z. Abdullah, S. Bhatia, Appl. Catal. B 100 (2010) 393–402.
- [5] V.M. Aroutiounian, V.M. Arakelyan, G.E. Shahnazaryan, Sol. Energy 78 (2005) 581–592.
- [6] C.G. Silva, M.J. Sampaio, R.R.N. Marques, L.A. Ferreira, P.B. Tavares, A.M.T. Silva, J.L. Faria, Appl. Catal. B 178 (2015) 82–90.
- [7] Z.G. Zou, J.H. Ye, K. Sayama, H. Arakawa, Nature 414 (2001) 625–627.
- [8] A. Kubacka, M.J. Muñoz-Batista, M. Fernández-García, S. Obregón, G. Colón, Appl. Catal. B 163 (2015) 214–222.
- [9] K. Villa, A. Black, X. Domenech, J. Peral, Sol. Energy 86 (2012) 558–566.
- [10] E.H. Kong, J. Lim, J.H. Lee, W. Choi, H.M. Jang, Appl. Catal. B 176 (2015) 76–82.
- [11] S. Obregón, M.J. Muñoz-Batista, M. Fernández-García, A. Kubacka, G. Colón, Appl. Catal. B 179 (2015) 468–478.
- [12] X.T. Hong, Z.P. Wang, W.M. Cai, F. Lu, J. Zhang, Y.Z. Yang, N. Ma, Y.J. Liu, Chem. Mater. 17 (2005) 1548–1552.
- [13] R. Asahi, T. Morikawa, T. Ohwaki, K. Aoki, Y. Taga, Science 293 (2001) 269–271.
- [14] G. Liu, Y. Zhao, C. Sun, F. Li, G.Q. Lu, H.M. Cheng, Angew. Chem. Int. Ed. 47 (2008) 4516–4520.
- [15] C.L. Li, J.A. Yuan, B.Y. Han, L. Jiang, W.F. Shangguan, Int. J. Hydrogen Energy 35 (2010) 7073–7079.
- [16] H. Park, W. Choi, M.R. Hoffmann, J. Mater. Chem. 18 (2008) 2379–2385.
- [17] G. Li, L. Wu, F. Li, P. Xu, D. Zhang, H. Li, Nanoscale 5 (2013) 2118–2125.
- [18] P.Y. Reddy, L. Giribabu, C. Lyness, H.J. Snaith, C. Vijaykumar, M. Chandrasekharan, M. Lakshmikantham, J.H. Yum, K. Kalyanasundaram, M. Grätzel, M.K. Nazeeruddin, Angew. Chem. Int. Ed. 46 (2007) 373–376.
- [19] D.F. Wang, J.H. Ye, H. Kitazawa, T. Kimura, J. Phys. Chem. C 111 (2007) 12848–12854.
- [20] D.F. Wang, J.H. Ye, T. Kako, T. Kimura, J. Phys. Chem. B 110 (2006) 15824–15830.
- [21] M. Tian, W. Shangguan, J. Yuan, L. Jiang, M. Chen, J. Shi, Z. Ouyang, S. Wang, Appl. Catal. A 309 (2006) 76–84.
- [22] W. Zhao, Y. Jin, C. Gao, W. Gu, Z. Jin, Y. Lei, L. Liao, Mater. Chem. Phys. 143 (2014) 952–962.
- [23] H.G. Kim, D. Hwang, J. Lee, J. Am. Chem. Soc. 126 (2004) 8912–8913.
- [24] M. Vehkamaeki, T. Hatanpaeae, M. Kemell, M. Ritala, M. Leskelae, Chem. Mater. 18 (2006) 3883–3888.
- [25] D.J. Singh, S.S.A. Seo, H.N. Lee, Phys. Rev. B 82 (2010) 180103.
- [26] S.E. Cummins, L.E. Cross, J. Appl. Phys. 39 (1968) 2268–2273.
- [27] Y. Liu, M.Y. Zhang, L. Li, X.T. Zhang, Appl. Catal. B 160 (2014) 757–766.
- [28] A. Kudo, S. Hiji, Chem. Lett. 28 (1999) 1103–1104.
- [29] W. Yao, H. Wang, X. Xu, S. Shang, Y. Hou, Y. Zhang, M. Wang, Mater. Lett. 57 (2003) 1899–1902.
- [30] W. Yao, X. Xu, H. Wang, J. Tao Zhou, X. Yang, Y. Zhang, S. Shang, B. Huang, Appl. Catal. B 52 (2004) 109–116.
- [31] W. Zhao, Z. Jia, E. Lei, L. Wang, Z. Li, Y. Dai, J. Phys. Chem. Solids 74 (2013) 1604–1607.
- [32] H. Zhang, M. Lu, S. Liu, L. Wang, Z. Xiu, Y. Zhou, Z. Qiu, A. Zhang, Q. Ma, Mater. Chem. Phys. 114 (2009) 716–721.
- [33] X. Lin, P. Lu, Q.F. Guan, H.B. Li, H. Li, J. Cai, Y. Zou, Acta. Phys. Chim. Sin. 28 (2012) 1978–1984.
- [34] X. Lin, Q.F. Guan, C.J. Zou, T.T. Liu, Y. Zhang, C.B. Lu, H.J. Zhai, Chin. J. Inorg. Chem. 29 (2013) 605–612.
- [35] H.J. Zhang, G. Chen, X. Li, Solid State Ion. 180 (2009) 1599–1603.

- [36] Z.W. Chen, H. Jiang, W. Jin, C. Shi, *Appl. Catal. B* 180 (2016) 698–706.
- [37] D.G. Calatayud, M. Rodriguez, B. Gallego, *Bol. Soc. Esp. Ceram. V* 51 (2012) 55–60.
- [38] T.L. Chang, W.T. Lin, *Appl. Surf. Sci.* 245 (2005) 376–383.
- [39] W. Zhao, Y. Jin, C. Gao, W. Gu, Z. Jin, Y. Lei, L. Liao, *Mater. Chem. Phys.* 143 (2014) 952–962.
- [40] J.F. Dorrian, R.E. Newnham, M.I. Kay, D.K. Smith, *Ferroelectrics* 3 (1971) 17–27.
- [41] H.F. Shi, H.Q. Tan, W.B. Zhu, Z.C. Sun, Y.J. Ma, E.B. Wang, *J. Mater. Chem. A* 3 (2015) 6586–6591.
- [42] W.J. Ren, Z.H. Ai, F.L. Jia, L.Z. Zhang, X.X. Fan, Z.G. Zou, *Appl. Catal. B* 69 (2007) 138–144.
- [43] W.E. Morgan, W.J. Stec an, J.R. Van Wazer, *J. Am. Chem. Soc.* 12 (1973) 751–755.
- [44] J.F. Moulder, W.F. Stickle, P.E. Sobol, K.D. Bomben, *Handbook of X-ray Photoelectron Spectroscopy*, Physical Electronics Inc. Press, Minnesoda, 1992.
- [45] C. Jovalekic, M. Pavlovic, P. Osmokrovic, L. Atanasoska, *Appl. Phys. Lett.* 72 (1998) 1051–1053.
- [46] M. Bowker, *Green Chem.* 13 (2011) 2235–2246.
- [47] H.J. Choi, M. Kang, *Int. J. Hydrogen Energy* 32 (2007) 3841–3848.
- [48] X. Yang, C. Salzmann, H. Shi, L. Malcolm, H. Green, T. Xiao, *J. Phys. Chem. C* 112 (2008) 10784–10789.
- [49] J. Chen, D.F. Ollis, W.H. Rulkens, H. Bruning, *Water Res.* 33 (1999) 669–676.
- [50] X.B. Chen, S.H. Shen, L.J. Guo, S.S. Mao, *Chem. Rev.* 110 (2010) 6503–6570.
- [51] C.S. Han, J. Andersen, V. Likodimos, P. Falaras, J. Linkugel, D.D. Dionysiou, *Catal. Today* 224 (2014) 132–139.
- [52] Y. Marcus, *The Properties of Solvents*, John Wiley & Sons, London, UK, 1998.
- [53] J. Choi, S.Y. Ryu, W. Balcerski, T.K. Lee, M.R. Hoffmann, *J. Mater. Chem.* 18 (2008) 2371–2378.
- [54] D.F. Hou, W. Luo, Y.H. Huang, J.C. Yu, X.L. Hu, *Nanoscale* 5 (2013) 2028–2035.
- [55] W. Wei, Y. Dai, B. Huang, *J. Phys. Chem. C* 113 (2009) 5658–5663.
- [56] S. Gupta, L. De Leon, V. Subramanian, *Phys. Chem. Chem. Phys.* 16 (2014) 12719–12727.
- [57] J.W. Tang, Z.G. Zou, J.H. Ye, *J. Phys. Chem. B* 107 (2003) 14265–14269.
- [58] R.J. Pei, Z.L. Cheng, E.K. Wang, X.R. Yang, *Biosens. Bioelectron.* 16 (2001) 355–361.
- [59] Y. Wang, F. Wang, J. He, *Nanoscale* 5 (2013) 11291–11297.
- [60] Y. Chen, H. Ge, L. Wei, Z. Li, R. Yuan, P. Liu, X. Fu, *Catal. Sci. Technol.* 3 (2013) 1712–1717.
- [61] S. Li, Y.H. Lin, B.P. Zhang, C.W. Nan, Y. Wang, *J. Appl. Phys.* 105 (2009) 056105.
- [62] K.V. Baiju, A. Zachariah, S. Shukla, S. Biju, M.L.P. Reddy, K.G.K. Warrier, *J. Phys. Chem. C* 111 (2007) 7612–7622.
- [63] Y. Sun, B.S. Eller, R.J. Nemanich, *J. Appl. Phys.* 110 (2011) 084303.
- [64] M.R. Hoffmann, S.T. Martin, W. Choi, D.W. Bahnemann, *Chem. Rev.* 95 (1995) 69–96.
- [65] D. Bockelmann, R. Goslich, D. Bahnemann, in: M. Becker, K.H. Funken, G. Schneider (Eds.), *Solar Thermal Energy Utilization*, vol. 6, Springer Verlag GmbH, Heidelberg, 1992, pp. 397–429.
- [66] E. Borgarello, J. Kiwi, M. Grätzel, E. Pelizzetti, M. Visca, *J. Am. Chem. Soc.* 104 (1982) 2996–3002.